

X-ray studies of the pulsar PSR J1420–6048 and its TeV pulsar wind nebula in the Kookaburra region

JAEGEUN PARK,¹ CHANHO KIM,¹ JOOYUN WOO,² HONGJUN AN,¹ KAYA MORI,² STEPHEN P. REYNOLDS,³ AND SAMAR SAFI-HARB⁴

¹*Department of Astronomy and Space Science, Chungbuk National University, Cheongju, 28644, Republic of Korea*

²*Columbia Astrophysics Laboratory, Columbia University, New York, NY 10027, USA*

³*Physics Department, NC State University, Raleigh, NC 27695, USA*

⁴*Department of Physics and Astronomy, University of Manitoba, Winnipeg, MB R3T 2N2, Canada*

ABSTRACT

We present a detailed analysis of broadband X-ray observations of the pulsar PSR J1420–6048 and its wind nebula (PWN) in the Kookaburra region with Chandra, XMM-Newton, and NuSTAR. Using the archival XMM-Newton and new NuSTAR data, we detected 68 ms pulsations of the pulsar and characterized its X-ray pulse profile which exhibits a sharp spike and a broad bump separated by ~ 0.5 in phase. A high-resolution Chandra image revealed a complex morphology of the PWN: a torus-jet structure, a few knots around the torus, one long ($\sim 7'$) and two short tails extending in the north-west direction, and a bright diffuse emission region to the south. Spatially integrated Chandra and NuSTAR spectra of the PWN out to $2.5'$ are well described by a power law model with a photon index $\Gamma \approx 2$. A spatially resolved spectroscopic study, as well as NuSTAR radial profiles of the 3–7 keV and 7–20 keV brightness, showed a hint of spectral softening with increasing distance from the pulsar. A multi-wavelength spectral energy distribution (SED) of the source was then obtained by supplementing our X-ray measurements with published radio, Fermi-LAT, and H.E.S.S. data. The SED and radial variations of the X-ray spectrum were fit with a leptonic multi-zone emission model. Our detailed study of the PWN may be suggestive of (1) particle transport dominated by advection, (2) a low magnetic-field strength ($B \sim 5\mu\text{G}$), and (3) electron acceleration to $\sim\text{PeV}$ energies.

1. INTRODUCTION

Ultra high-energy cosmic rays (UHECRs) with energies of $\gtrsim 10^{20}$ eV are detected on Earth, but their origin remains unclear. It is well known that very high-energy cosmic-ray electrons ($\lesssim 10^{15}$ eV) are produced in pulsar-wind nebulae (PWNe) as evidenced by their TeV emission. Acceleration of particles to very high energies in PWNe is thought to occur at the termination shocks of their relativistic winds (Kennel & Coroniti 1984). The particles flow outwards and form an extended bubble of synchrotron radiation via interaction with a magnetic field (B) as observed in the radio to X-ray band. The particles can inverse-Compton upscatter (ICS) the synchrotron, CMB, and/or infrared (IR) photons to produce VHE emission (e.g., Harding 1996). This synchrotron-ICS emission scenario has been widely employed in models of PWN emission and has provided useful information on particle acceleration and transport

in PWNe (e.g., Gelfand et al. 2009; Bucciantini et al. 2011).

Observatories operating at ultra-high TeV energies (e.g., Lhaaso Collaboration et al. 2021) have revealed numerous TeV PWNe that can provide insights into cosmic PeVatrons, or the origin of cosmic rays at energies of $\sim 10^{15}$ eV. Hence, studies of PeV cosmic-ray electrons have been done primarily with observations of very high-energy (VHE; >100 GeV) radiation from these PWNe and their surrounding halos (e.g., H. E. S. S. Collaboration et al. 2018). In particular, very high-energy particles in PWNe with ages of ~ 10 – 100 kyr may escape from the compact PWNe into the interstellar medium, propagate towards Earth, and be detected as high-energy cosmic rays (e.g., Giacinti et al. 2020).

While VHE emission of PWNe is certainly a useful probe to explore particle acceleration and propagation, properties of the particles at the highest energies cannot be precisely characterized by VHE spectra alone because their emission spectra can be distorted by Klein-Nishina suppression (Klein & Nishina 1929).

Corresponding author: Hongjun An
hjan@cbnu.ac.kr

Besides, modeling the VHE emission requires knowledge of the ambient IR seed photon sources, which typically have poorly known temperature and density profiles. On the contrary, synchrotron emissions of PWNe do not suffer from the aforementioned effects and thus provide a complementary tool for investigating particle acceleration and transport in PWNe (e.g., Reynolds 2016). The highest-energy particles (in TeV–PeV energies) emit synchrotron photons in the X-ray to MeV band, and hence X-ray data are crucial to understanding UHECRs in PWNe (e.g., Mori et al. 2021; Burgess et al. 2022).

The point source PSR J1420–6048 (J1420 hereafter) and surrounding PWN-like emission were discovered by targeted X-ray observations of an EGRET source (Roberts & Romani 1998; Roberts et al. 2001b) in the so-called ‘Kookaburra’ region (Roberts et al. 1999). Radio pulsations with a period of 68 ms were detected from J1420 (D’Amico et al. 2001); the radio pulsar, whose characteristic age (τ_c) is 13 kyr, is very energetic, with a high spin-down luminosity (\dot{E}_{SD}) of 10^{37} erg s $^{-1}$. The discovery of the pulsations firmly established the association between J1420 and the nebula detected in the radio and X-ray bands (the ‘K3’ PWN; Roberts et al. 1999, 2001a). D’Amico et al. (2001) estimated the distance to the pulsar to be 7.7 kpc based on dispersion measure (DM), while 5.6 kpc was later suggested using a different DM model (Ng et al. 2005). Gamma-ray pulsations of J1420 were detected with high significance (Weltevrede et al. 2010)¹ but an X-ray detection of the pulsations made with ASCA data was only marginal with a chance probability of $p = 0.0056$ (Roberts et al. 2001a). The X-ray pulsations have not been confirmed by later studies (Ng et al. 2005; Kuiper & Hermsen 2015). These previous attempts to find X-ray pulsations seem to be hampered by the lack of photon statistics and/or strong contamination from the PWN.

Multi-band studies have been carried out to understand the K3 PWN. Roberts et al. (1999) and Van Etten & Romani (2010) measured radio flux densities of the source, and its X-ray spectrum with a photon index $\Gamma \approx 2$ was seen to soften with increasing distance from the pulsar (Van Etten & Romani 2010; Kishishita et al. 2012). Aharonian et al. (2006) discovered an extended TeV source coinciding with K3 (but with an offset center) and measured a $\Gamma = 2.2$ power-law spectrum in the TeV band. Van Etten & Romani (2010) modeled the broadband SEDs of an inner region and an extended nebula of K3 using a two-zone time-dependent

emission model. They found that a leptonic scenario provides a better fit to the SEDs than a hadronic hybrid model. In multi-band images, Van Etten & Romani (2010) identified an apparent radio shell structure and a long 8’ X-ray tail in the north. These images suggest that the pulsar was born 3’ northwest of its current position at the center of the apparent radio shell, and electrons spewed by the pulsar produce the X-ray tail and offset TeV emission via the synchrotron and ICS emission, respectively.

In this paper, further X-ray investigations along with modeling multi-band SED and X-ray morphology data are attempted to understand the K3 PWN’s properties better. We describe data reduction processes in Section 2.1, and present the data analyses and results in Section 2.2–2.4. We then apply a multizone model to the broadband SED and radial profiles, and infer the properties of the source (Section 3). We discuss the results in Section 4 and summarize in Section 5.

2. X-RAY DATA ANALYSIS

2.1. Data reduction

We analyzed archival Chandra and XMM-Newton data acquired on 2010 December 8 for 90 ks (Obs. ID 12545) and on 2018 February 19 for 91 ks (Obs. ID 0804250501), respectively, and a new NuSTAR observation acquired on 2021 May 11 for 130 ks (Obs. ID 40660002002; Mori et al. 2021). We reprocessed the Chandra data using `chandra_repro` of CIAO 4.14 along with CALDB 4.9.6 for the most recent calibration data. The XMM-Newton data were processed with the `emproc` and `epproc` tasks of SAS 20211130_0941. Since the XMM-Newton observation data were severely affected by particle flares, we used tight flare cuts (e.g., `RATE<=0.1`) which reduce the exposures substantially to <40 ks. Still, the data suffer from some contamination by residual flares, which could be a concern for spectral analysis of the faint and extended PWN. The flare background is less concerning for timing analysis of the pulsar, so we perform timing analysis with the PN data after applying a more typical flare cut of `RATE<=0.4`.² The NuSTAR data were reduced with `nupipeline` in HEASOFT v6.29 using the `SAA_MODE=strict` flag as recommended by the NuSTAR science operation center. We verified that using `SAA_MODE=optimized` did not change the results significantly (but see Section 2.2). Net exposures after this reduction are 90 ks, 65 ks, and 57 ks for Chandra, XMM-Newton/PN, and NuSTAR, respec-

¹ https://www.slac.stanford.edu/~kerrm/fermi-pulsar_timing/

² <https://www.cosmos.esa.int/web/xmm-newton/sas-thread-epic-filterbackground>

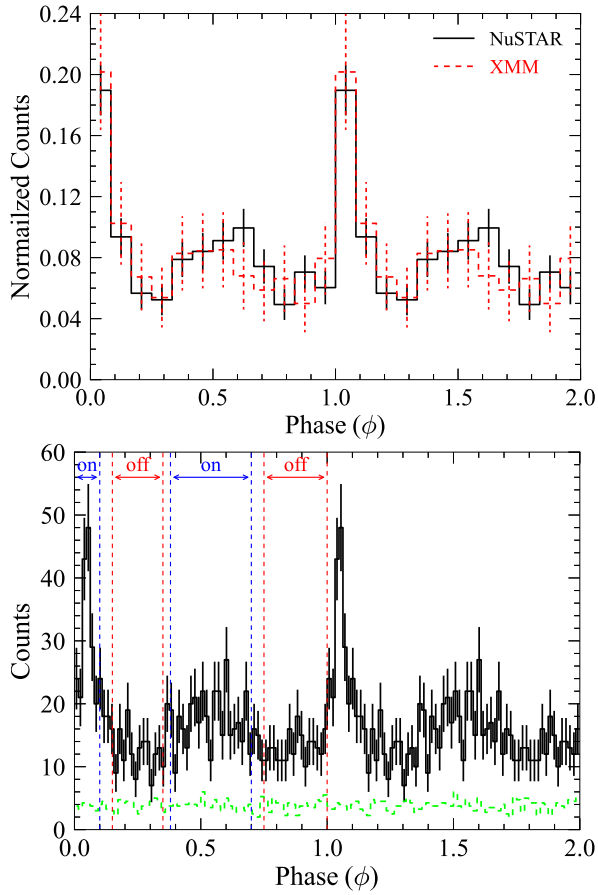


Figure 1. *Top:* 1–10 keV XMM-Newton (red) and 3–30 keV NuSTAR (black; FPMA and FPMB combined) pulse profiles. The XMM-Newton profile was constructed using photon weights (see text), and the background was subtracted from the NuSTAR profile. The profiles were normalized to have a summed count of 1, and reference phases of the profiles were adjusted to align them. *Bottom:* 3–30 keV NuSTAR profiles of the source (black) and background (green) events measured using finer bins.

tively. Note that all errors reported in this paper are 1σ .

2.2. Detection of the pulsations of J1420

We searched the X-ray data for 68-ms pulsations of J1420 to confirm an earlier X-ray detection which was only suggestive (Roberts et al. 2001a). For the XMM-Newton data, we extracted 1–10 keV events within a $R = 16''$ circle centered at the pulsar position of (R.A., decl.)=(215.034142°, -60.804124°) (D’Amico et al. 2001) and applied a barycentric correction to the event arrival times. We then folded the arrival times using a range of test frequencies ($f = 14.656955$ – 14.657095 Hz) around one obtained by extrapolating the timing solution (Kerr et al. 2015) obtained by the Fermi Large Area Telescope (LAT; Atwood et al. 2009), and computed an H statistic (de Jager et al. 1989) for

each test frequency. In this search, we held the frequency derivative \dot{f} fixed at the LAT-measured value of $\dot{f} = -1.772 \times 10^{-11}$ Hz s $^{-1}$. This search resulted in a significant detection at $f = 14.657082$ Hz (MJD 58168) with $H \approx 40$, corresponding to a post-trial chance probability of $p \approx 5 \times 10^{-7}$. The detection significance changes substantially between $H \approx 30$ and $H \approx 60$ depending on the region selection, presumably because of strong PWN emission.

In order to mitigate contamination by the PWN, we adopted a weighted H test (Kerr 2011), for which the probability of each event being a source photon is computed by fitting an image of a region around J1420 with the point spread function (PSF) plus a constant. This yielded more stable (reliable) detection of the pulsations with $H \approx 50$ – 60 , corresponding to a post-trial $p \approx 10^{-9}$, regardless of the region selection as long as the region size was reasonable (e.g., $R \geq 10''$). The probability-weighted 1–10 keV pulse profile is displayed in Figure 1 (top).

We expected that X-ray pulsations might be more easily detected in the NuSTAR data since the pulsar’s spectrum was inferred to be hard ($\Gamma \approx 0.5$; Kuiper & Hermsen 2015). In NuSTAR images (Section 2.3.2), excess emission at the pulsar position was noticeable up to ~ 30 keV whereas the extended PWN was not significantly detected at energies above 20 keV, meaning that the pulsar emission is spectrally harder than the PWN emission. We therefore used the 3–30 keV and 3–20 keV bands for the pulsar and the PWN emission (e.g., Section 2.4.2), respectively. We extracted 3–30 keV source events within a $R = 30''$ circle centered at the brightest spot in the 10–30 keV smoothed images, and performed an H test in a range of f (14.655187–14.655320 Hz) holding \dot{f} fixed at the LAT-measured value. Source pulsations with $f = 14.655289$ Hz on MJD 59345 were more significantly detected in the NuSTAR data ($H \approx 100$ corresponding to a post-trial $p = 6 \times 10^{-17}$) than in the XMM-Newton data. The XMM-Newton and NuSTAR measurements of f yielded an average frequency derivative of -1.763×10^{-11} Hz s $^{-1}$ which is similar to that measured by Fermi-LAT. The 3–30 keV pulse profile is displayed in Figure 1. We also checked to see if the pulsations persist at >20 keV. While the 20–30 keV pulse profile seemed to show a hint of the pulsations, the detection significance was low ($H \leq 10$), likely due to the paucity of counts. We therefore relaxed the SAA.MODE cut (from strict to optimized³)

³ https://heasarc.gsfc.nasa.gov/docs/nustar/analysis/nustar_sw_guide.pdf

and were able to detect the 20–30 keV pulsations significantly with $H \approx 20$ ($p \approx 3 \times 10^{-4}$).

We arbitrarily adjusted the reference phases of the XMM-Newton and NuSTAR profiles to align their peaks, and display them in Figure 1. The profiles show a sharp peak at phase $\phi \approx 0.05$ and a broad bump (Fig. 1). The bump is visible in both the XMM-Newton and NuSTAR data, but a constant function can fit the profiles in the phase interval for the bump ($\phi = 0.25$ – 0.9) with $p=0.01$ and 0.9 for the NuSTAR and XMM-Newton profile, respectively; the existence of the broad bump is not definitive. A further investigation of the profile with the high timing resolution NuSTAR data revealed that the sharp peak is indeed narrow ($\Delta\phi \lesssim 0.1$; Fig. 1 bottom).

2.3. Image analysis

Previous Suzaku studies of K3 (Van Etten & Romani 2010; Kishishita et al. 2012) found that the source is elongated to the north where an apparent radio shell lies (Van Etten & Romani 2010). On a smaller scale, Ng et al. (2005) found an X-ray arc in 10 ks Chandra data (Obs. ID 2792) and suggested that it could be the termination shock. Moreover, the spectral softening detected in K3 (Van Etten & Romani 2010; Kishishita et al. 2012) may be manifested by a size shrinkage with increasing energy (e.g., Nynka et al. 2014; An et al. 2014a). In this section, we inspect the Chandra data to identify the small- and large-scale structures, and analyze the NuSTAR data to measure the size shrinkage of K3.

2.3.1. Chandra images

We produced a Chandra image in the 2–7 keV band after removing point sources and correcting for exposure. This was done by following a procedure in the CIAO science thread.⁴ We then adjusted the image scales and bins to identify structures in the PWN on various spatial scales (Fig. 2).

On a $40'' \times 40''$ scale, we identified two knots at $3''$ and $7''$ from the pulsar (Knot 1 and Knot 2; Fig. 2 a); compared to nearby backgrounds, the knots were detected at $\sim 3\sigma$ significance. Note that Knot 1 is listed in the Chandra source catalog⁵, but we do not find an IR or optical counterpart in the 2MASS and USNO catalogs. Furthermore, the knots appear to be more extended than nearby point sources with similar counts. Note also that there seems to be a slightly elongated structure (short and parallel to but just east of the jet indicated in Fig-

ure 2b), but this structure was detected only at the 2.5σ level. An image of a $2' \times 2'$ region near the pulsar is displayed in Figure 2b. In this image, the torus structure in the east-west direction identified by Ng et al. (2005) is clearly visible. In addition, we found a narrow jet-like ($\sim 20''$) feature extending in the north-east direction. The jet-like structure is fainter but detected at a $\geq 3\sigma$ level, having 172 events in the 1–10 keV band within a $7'' \times 17''$ ellipse (excluding the pulsar and torus emission; Fig. 2 b) which contains estimated 119 background counts.

A larger-scale image is displayed along with VHE emission regions (H. E. S. S. Collaboration et al. 2018; Abdollahi et al. 2020) in Figure 2 c. The image reveals a prominent $\sim 7'$ tail (denoted as ‘Tail’) and two short tails in the north-west direction. These tails seem to constitute the broad northern tail observed in the low-resolution Suzaku image (Van Etten & Romani 2010; Kishishita et al. 2012). In the south, a bright emission region is seen out to $\sim 2.5'$. The bright southern region and the northern ‘Tail’ were also identified in our inspection of XMM-Newton MOS images. The ‘Tail’ appears to partially overlap with a radio structure (Fig. 2 d; see also Van Etten & Romani 2010).⁶ The VHE emission regions are centered at 2–3' north of the pulsar (white and cyan circles in Fig. 2 c) and also overlap well with the X-ray PWN. Note also that there is weak excess emission in the southwest (near the chip boundary). This region is 15–20% brighter than other background regions, possibly indicating inhomogeneous sky emission on a larger scale as was seen in an ASCA image (e.g., Roberts et al. 2001b).

We also searched the Chandra images for a shell-like structure (e.g., supernova remnant) in several energy bands but did not find any. Additionally, we compared spectra of various regions within the FoV with blank-sky data⁷ to see if there is an excess of line emission but found none.

2.3.2. NuSTAR image

We next produced 3–7 keV and 7–20 keV NuSTAR images of the source. To take into account the spatially non-uniform background, we carried out `nuskybgd` simulations.⁸ Although the simulated background images reproduced the aperture patterns well, the normalization of the simulated image differed from the observed

⁴ https://cxc.cfa.harvard.edu/ciao/threads/diffuse_emission/

⁵ <https://cxc.cfa.harvard.edu/csc/>

⁶ see <https://skyview.gsfc.nasa.gov/current/cgi/moreinfo.pl?survey=SUMSS%20843%20MHz> for more information on the radio image

⁷ <https://cxc.cfa.harvard.edu/ciao/threads/acisbackground/>

⁸ <https://github.com/NuSTAR/nuskybgd>

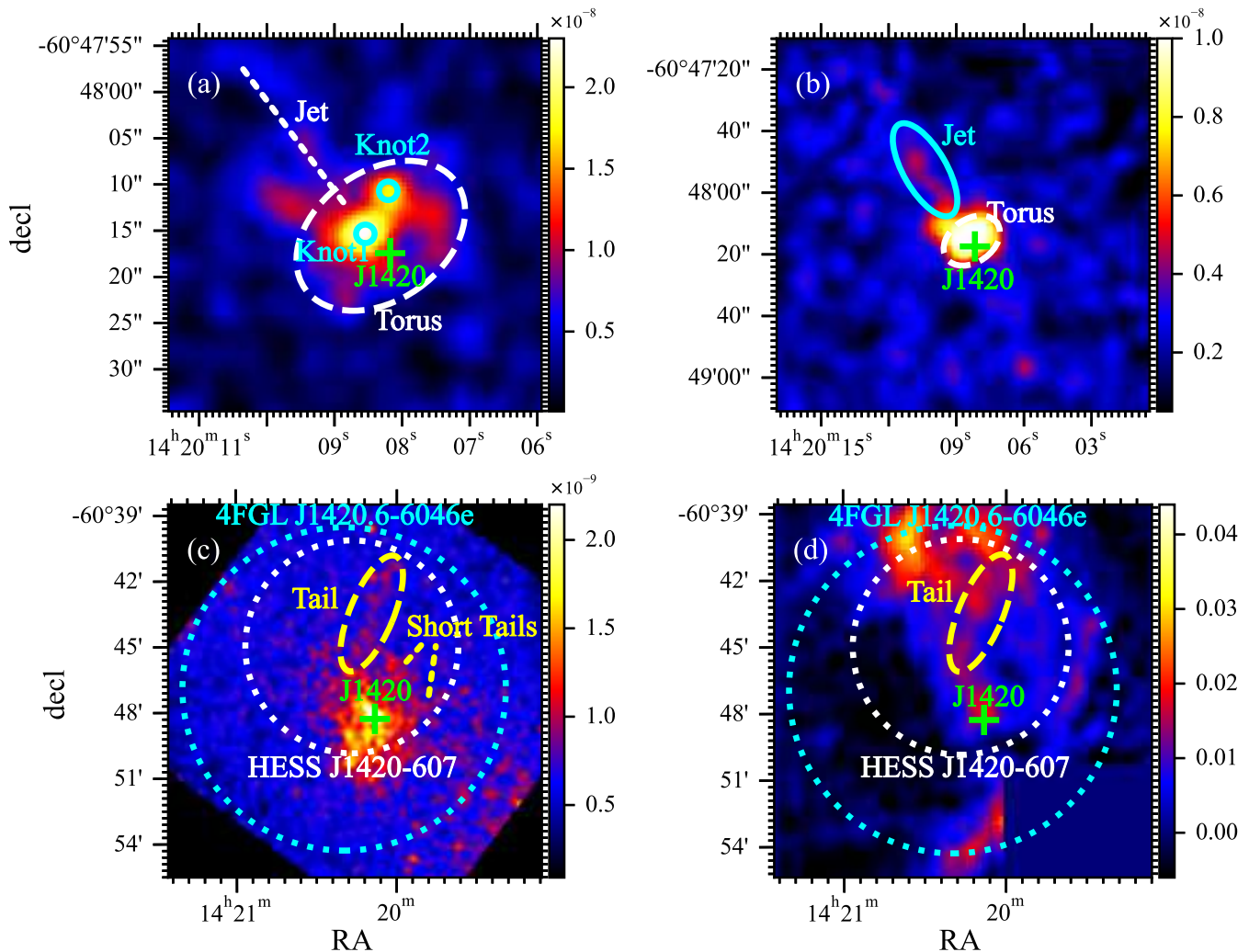


Figure 2. 2–7 keV Chandra images of the K3 PWN on various spatial scales (a–c) and a SUMSS 843 MHz image (d). The images are smoothed and the scales are adjusted for better legibility. The point-source-removed and exposure-corrected Chandra images are constructed following a CIAO science thread. The position of J1420 is denoted by a green cross. (a) Chandra image on a $40'' \times 40''$ scale. In addition to the two knots denoted in cyan, a faint jet (not visible in this panel) and a torus are marked. (b) Chandra image on a $2' \times 2'$ scale. The torus and the jet structures are shown in white and cyan ellipses, respectively. (c) Chandra image on a $16' \times 16'$ scale. A long northern tail region is denoted by a yellow ellipse and two short tails are marked. Regions of the Fermi-LAT (0.123° ; radius of a disk model) and H.E.S.S. (0.08° ; 1σ width of a Gaussian model) counterparts are displayed in cyan and white circles, respectively. (d) SUMSS 843 MHz image (Mauch et al. 2003). The image was downloaded from the Skyview webpage and truncated to match the X-ray emission region in panel (c). Note also that a box region in the lower right corner is excised because it contains a bright unrelated point source. The pulsar, northern X-ray tail, and Fermi-LAT and H.E.S.S. regions are overlaid for comparison.

one by $<10\%$ in each chip. Hence, we manually adjusted the background normalization to match the observed background counts in each chip. We combined FPMA and FPMB images after aligning them using the brightest spot in the 10–30 keV smoothed images (Section 2.2). Background-subtracted NuSTAR images of the K3 PWN show primarily the bright southern region (Fig. 3), and the low- and high-energy morphologies do not appear significantly different.

We produced 3–7 keV and 7–20 keV radial profiles to further investigate possible size shrinkage of K3 with

energy. Although contamination from the pulsar can be minimized by pulse gating, the statistics would then be insufficient for a meaningful comparison because the off-pulse intervals are narrow ($\Delta\phi < 0.5$; Fig. 1 top). Therefore, we used all the pulse phases. Radial profiles in the low- and high-energy bands along with simulated background profiles are displayed in the top panel of Figure 3 c; the background profiles account for the observations at large radii as expected. To assess the relative contributions of the pulsar and extended emission, we fit the radial profile with a model composed

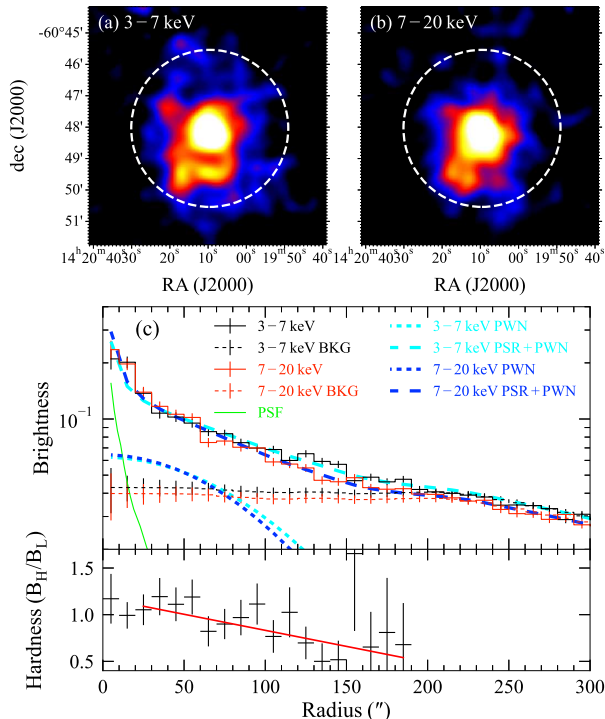


Figure 3. Background-subtracted NuSTAR images (a–b) and radial profiles (c) in the 3–7 keV and 7–20 keV bands. (a–b) NuSTAR images in the 3–7 keV (a) and 7–20 keV bands (b). The images are smoothed and normalized to 1 at the maximum counts, and $R = 2.5'$ circles are shown for reference. The image scales are adjusted for legibility. (c) 3–7 keV (black) and 7–20 keV (red) radial profiles of surface brightness (counts per area) are presented in the top panel. The green line is the radial profile of the PSF (pulsar), and the black and red dotted lines are background profiles in the low and high-energy bands, respectively. Radial Gaussian functions that describe the PWN profiles in the low- and high-energy bands are shown in cyan and blue dotted lines, respectively. The summed models are presented in the cyan and blue dashed lines for the low- and high-energy profiles, respectively. Hardness ratios, defined by the high-energy to low-energy brightness ratio, are displayed in the bottom panel, and the red line is a linear fit to the hardness ratios.

of the PSF (pulsar), background, and a Gaussian function $A\exp(-r^2/2w^2)$ (PWN); the best-fit functions are displayed in Figure 3 c. The inferred normalization factors for the background profiles were consistent with 1 at $\lesssim 1\sigma$ level, and the pulsar flux was estimated to be $\approx 10\%$ of the PWN flux (see also Table 1) and dominates only in the innermost regions $r < 20''$ (Fig. 3 c).

The widths (w) of the best-fit Gaussian functions for the low- and high-energy profiles were determined to be $82 \pm 3''$ and $75 \pm 2''$, respectively. The measured widths differ only at the 1.6σ level and thus do not clearly require a size shrinkage with energy. Because the synchrotron burn-off effects should also produce spectral softening with increasing radius, we computed hardness

ratios (ratio of the hard- and soft-band brightness) and show them in the bottom panel of Figure 3 c. The hardness ratio nearly monotonically decreases out to $\sim 200''$ beyond which the background dominates. A linear fit to the hardness ratios ($20'' \leq r \leq 190''$) found a negative slope (i.e., spectral softening) at the $\approx 3\sigma$ level with $\chi^2/\text{dof} = 10/17$ (red line in the bottom panel of Fig. 3 c). Note, however, that the negative slope might be caused primarily by the two data points at $R = 130''\text{--}140''$, rather than by a gradual decrease. Ignoring the two points reduced the significance to a $\approx 2\sigma$ level, which still hints at a gradual decrease although a firm conclusion on the softening cannot be made with the current data.

2.4. Spectral analysis

In this section, we analyze X-ray spectra of the K3 PWN and its sub-structures that were identified in the Chandra images (Fig. 2). The spectral softening measured for K3 (Van Etten & Romani 2010; Kishishita et al. 2012) implies a spectral curvature in its spatially integrated spectrum which may be detected in the broadband X-ray data taken with NuSTAR (e.g., Madsen et al. 2015a). Furthermore, the NuSTAR data may allow the detection of a spectral cut-off at $>10\text{ keV}$ (e.g., An 2019). Because other point sources within the PWN may contaminate the NuSTAR spectra of the PWN, we estimate the contributions from the point sources using the high-resolution Chandra data.

2.4.1. Point sources within the PWN

In the image analysis (Section 2.3.1), we detected 10 point sources and the pulsar J1420 within a $R = 2.5'$ circle centered at the pulsar, using the `wavdetect` tool of CIAO. The point sources seen in the Chandra image are very faint, having 10–20 events within $R = 2''$ regions compared to 260 events for J1420. With so few counts, accurate spectral characterization of each source was unfeasible. However, these faint sources are unlikely to affect NuSTAR measurements of the PWN spectra (Sections 2.4.2 and 2.4.4). For a better assessment, we stacked the Chandra spectra of the 10 point sources using $R = 2''$ extraction regions. A summed background spectrum was constructed using $R = 3''$ circles near the source regions. We grouped the stacked spectrum to have at least 5 counts per bin and fit the spectrum with an absorbed power-law model employing the l statistic (Loredo 1992). For the Galactic absorption, we adopted the `tbabs` model along with the `vern` cross section (Verner et al. 1996) and `angr` abundances (Anders & Grevesse 1989) in XSPEC v12.12.0 (throughout this paper). Although the hydrogen column density N_{H} was not well constrained, the model fit favored a

Table 1. Spectral analysis results

data	Instrument ^a	energy range (keV)	N_{H} (10^{22} cm^{-2})	Γ	$F_{3-10 \text{ keV}}$ ($10^{-13} \text{ erg s}^{-1} \text{ cm}^{-2}$)	χ^2/dof
PSR ^b	C	0.5–10	4.6 ^c	0.7 ± 0.2	$1.3^{+0.2}_{-0.1}$	30/46
PSR ^d	N	3–30	4.6 ^c	0.7 ± 0.4	$1.5^{+0.6}_{-0.4}$	21/22
PWN ^e	C	0.5–10	$4.2 \pm 0.5 \pm 0.4$	$1.82 \pm 0.23 \pm 0.11$	$15.3 \pm 0.9 \pm 0.4$	156/146
PWN ^e	N	3–20	4.2 ^f	$1.97 \pm 0.06^{+0.08}_{-0.07}$	$16.5 \pm 0.6 \pm 0.6$	168/170
PWN ^e	C+N	0.5–20	$4.6 \pm 0.3 \pm 0.4$	$1.98 \pm 0.07^{+0.08}_{-0.06}$	$15.0 \pm 0.7 \pm 0.3$	324/317
Torus	C	0.5–10	4.6 ^c	1.8 ± 0.3	0.7 ± 0.1	6/10
Jet	C	0.5–10	4.6 ^c	2.1 ± 0.7	0.2 ± 0.1	4/5
Tail	C	0.5–10	4.6 ^c	2.06 ± 0.26	$3.5^{+0.5}_{-0.4}$	134/120

^aC: Chandra, N: NuSTAR.

^bOn+off pulse emission.

^cFixed at the value obtained from a joint fit of the Chandra+NuSTAR PWN spectra.

^dOn–off pulse emission.

^eThe second error is a systematic uncertainty. See text for more detail.

^fFixed at the Chandra-measured value.

very low value (consistent with 0) perhaps because of low-energy emission from a few soft, foreground sources – these soft X-ray sources do not have a significant contribution to $>3 \text{ keV}$ NuSTAR spectra. We, therefore, set N_{H} to 0 and found that a power law model with a photon index of 1.2 ± 0.2 and absorption-corrected 3–10 keV flux $F_{3-10 \text{ keV}} = 2.3^{+0.6}_{-0.5} \times 10^{-14} \text{ erg cm}^{-2} \text{ s}^{-1}$ fits the data; the latter is $\leq 2\%$ of the PWN flux (see below). Note that using a larger N_{H} makes Γ softer (i.e. fewer counts in the NuSTAR band) and thus our estimation above is conservative.

To measure the pulsar spectrum with the Chandra data, we extracted events within a $R = 2''$ circle centered at the pulsar position. A background spectrum was extracted within two $R = 2''$ circles in the torus region. We grouped the source spectrum to have a minimum of 5 counts per spectral bin and employed the l statistic in the fit. The spectrum was well fit with an absorbed power-law model for a frozen $N_{\text{H}} = 4.6 \times 10^{22} \text{ cm}^{-2}$ which was obtained from a joint fit of the Chandra+NuSTAR PWN spectra of a large region (see Section 2.4.2). The fit resulted in $\Gamma = 0.7 \pm 0.2$ and $F_{3-10 \text{ keV}} = 1.3 \times 10^{-13} \text{ erg cm}^{-2} \text{ s}^{-1}$ (Fig. 4). Note that Kuiper & Hermsen (2015), using a likelihood method applied to the same Chandra data, obtained $\Gamma = 0.46 \pm 0.07$ for $N_{\text{H}} = 3.35^{+0.74}_{-0.51} \times 10^{22} \text{ cm}^{-2}$. The difference in the measured photon indices seems to arise from its covariance with N_{H} ; by fixing N_{H} to $3.35 \times 10^{22} \text{ cm}^{-2}$, the photon index was fit to $\Gamma = 0.4 \pm 0.2$, consistent with the results in Kuiper & Hermsen (2015).

We also measured the pulsed spectrum of J1420 using the NuSTAR data. We extracted source events within a $R = 30''$ circle around the pulsar position and selected on- ($\phi=0-0.1$ and $0.38-0.7$; Fig. 1) and off-pulse ($\phi=0.15-0.35$ and $0.75-1.00$) data for the source and background spectrum, respectively. The pulsed

(on–off) spectrum was fit with an absorbed power-law model in the 3–30 keV band, and we found the best-fit parameters to be $\Gamma = 0.7 \pm 0.4$ and $F_{3-10 \text{ keV}} = 1.5^{+0.6}_{-0.4} \times 10^{-13} \text{ erg cm}^{-2} \text{ s}^{-1}$. The latter becomes $F_{3-10 \text{ keV}} = 6^{+3}_{-2} \times 10^{-14} \text{ erg cm}^{-2} \text{ s}^{-1}$ when averaged over a spin cycle (Fig. 4).

2.4.2. Spatially integrated PWN spectrum

To construct a broadband X-ray SED to be used in our SED modeling (Section 3), we measured the spatially integrated spectra of the PWN with the Chandra and NuSTAR data. For the Chandra analysis, we extracted the source spectrum within a $R = 2.5'$ circle centered at the pulsar, excising the pulsar and other point sources (Section 2.4.1) using $R = 2''$ circles. This PWN region contains most of the bright nebula, but the outer part of the long ‘Tail’ is not included (see Section 2.4.3 for the tail spectrum). Because background selection for the faint and extended nebula was a concern, we used the blank-sky data to choose optimal background regions by comparing the blank-sky background and the observed image. We note that the source region lies across four detector chips, and hence we adjusted the background region sizes taken in the four chips so that the sizes are approximately proportional to the source-region areas within the corresponding chips. We verified that the blank-sky data explained well the instrumental line emissions (e.g., Bartalucci et al. 2014) in the source and background regions and that the source and background spectra (including instrumental lines) agreed very well in the low- ($\lesssim 1.5 \text{ keV}$) and high-energy ($\gtrsim 7 \text{ keV}$) bands, meaning that the background represents well the detector and sky background in the source region.

We generated response files for the extended source region using the `specextract` tool of CIAO, grouped the spectrum to have a minimum of 100 counts

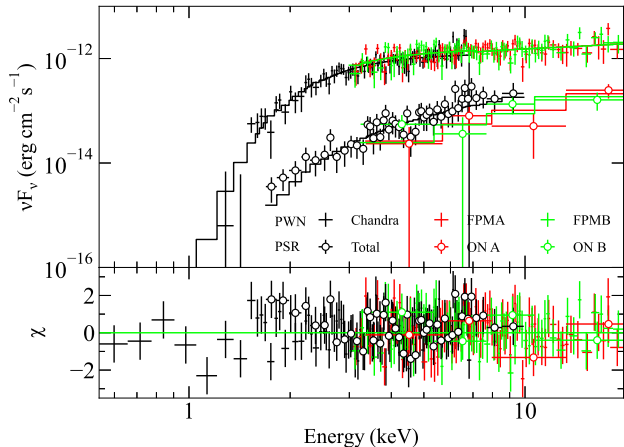


Figure 4. Chandra (black) and NuSTAR (red and green) spectra of J1420 (empty circles) and the K3 PWN (crosses). The NuSTAR spectra of the pulsar were generated in the on-pulse phases by subtracting the off-pulse background and were averaged over the spin cycle. Best-fit models are presented as solid lines.

per spectral bin, and fit the 0.5–10 keV spectrum with an absorbed power-law model (Fig. 4). This model adequately describes the observed spectrum ($\chi^2/\text{dof}=156/146$), and the fit-inferred parameter values are $N_{\text{H}} = (4.2 \pm 0.5) \times 10^{22} \text{ cm}^{-2}$, $\Gamma = 1.82 \pm 0.23$, and $F_{3-10 \text{ keV}} = (1.53 \pm 0.09) \times 10^{-12} \text{ erg cm}^{-2} \text{ s}^{-1}$. These N_{H} and Γ values are similar to the previous measurements of Van Etten & Romani (2010) and Kishishita et al. (2012). Note, however, that they did not report the Galactic abundance and scattering cross-section used for their absorption models, and thus we assumed that they used the `vern` cross-section and `angr` abundances (the default in XSPEC). The PWN spectrum is better constrained by combining it with the NuSTAR data below.

As noted above, the Chandra-only fit results may significantly vary depending on the background selection, especially because of the covariance between N_{H} and Γ . Therefore, we analyzed the data with 10 different background selections to estimate systematic uncertainties (i.e., 1σ variation) and found that the best-fit parameters change by $\Delta N_{\text{H}} = \pm 4 \times 10^{21} \text{ cm}^{-2}$, $\Delta \Gamma = \pm 0.11$, and $\Delta F_{3-10 \text{ keV}} = \pm 4 \times 10^{-14} \text{ erg cm}^{-2} \text{ s}^{-1}$. We report these systematic uncertainties as additional errors in Table 1.

To measure the NuSTAR spectrum of the PWN, we used $R = 2.5'$ circles for extraction of the source spectra (Fig. 4). As noted above, the NuSTAR background is non-uniform, and thus it was difficult to extract local background spectra on the same detector chip, especially for FPMA. We therefore used the `nuskybgd` simulations (Wik et al. 2014) to generate a background spectrum

corresponding to the source region for each of FPMA and FPMB. We verified that the background model adequately explained the observed background spectra as well as the high-energy background ($>30 \text{ keV}$) in the source spectra.

Because the pulsar emission was included in our phase-integrated NuSTAR spectra, we modeled those spectra with two power laws, one for the PWN and the other for the pulsar emission. We held the second power-law parameters fixed at Chandra-measured pulsar parameters and fit the 3–20 keV source spectra holding N_{H} fixed at $4.2 \times 10^{22} \text{ cm}^{-2}$. An acceptable fit ($\chi^2/\text{dof}=168/170$) was achieved with the best-fit parameters of $\Gamma = 1.97 \pm 0.06$ and $F_{3-10 \text{ keV}} = (1.65 \pm 0.06) \times 10^{-12} \text{ erg cm}^{-2} \text{ s}^{-1}$. The NuSTAR-measured flux and photon index are consistent with the Chandra-measured ones at the $\sim 1\sigma$ level. To check this further, we inspected the NuSTAR spectra in the 3–10 keV band and found that the fit-inferred PWN $\Gamma = 1.92 \pm 0.10$ is still consistent with the Chandra measurement. We also attempted to fit the 3–20 keV PWN spectra with a broken power-law model and found that a spectral break is not statistically required with an f -test probability of ≈ 0.5 .

We assessed systematic uncertainties on the NuSTAR-inferred parameters. The NuSTAR fit results are not very sensitive to a modest change of N_{H} ; varying it within the Chandra-estimated uncertainty of $\pm 7 \times 10^{21} \text{ cm}^{-2}$ (Table 1) changes Γ by ± 0.04 and $F_{3-10 \text{ keV}}$ by $\pm 5 \times 10^{-14} \text{ erg cm}^{-2} \text{ s}^{-1}$ (min/max). The assumed pulsar spectral model may also introduce some uncertainties in the inferred spectral parameters. We therefore varied the pulsar model within the measurement uncertainties considering the covariance between Γ and $F_{3-10 \text{ keV}}$ of the pulsar. We found that the effects of the pulsar model are not significant; Γ varies by $+0.05$ and -0.03 , and the change of $F_{3-10 \text{ keV}}$ is $\Delta F_{3-10 \text{ keV}} = \pm 10^{-14} \text{ erg cm}^{-2} \text{ s}^{-1}$ (min/max). We also varied background regions for the `nuskybgd` simulations (see Wik et al. 2014, for more detail), generated 20 background spectra, and used them in our spectral fits. The best-fit parameters vary depending on the background used: $\Delta \Gamma = \pm 0.04$ and $\Delta F_{3-10 \text{ keV}} = \pm 3 \times 10^{-14} \text{ erg cm}^{-2} \text{ s}^{-1}$ (standard deviations; 1σ). We combine these systematic uncertainties in quadrature and report them in Table 1 (second errors).

To measure the PWN spectrum accurately, we jointly fit the 0.5–10 keV Chandra and 3–20 keV NuSTAR spectra of the PWN (Fig. 4 and Fig. 5 a). Note that we modeled the Chandra spectrum with a single power law and the NuSTAR spectra with two power laws with

the second power law representing the pulsar emission (fixed to the Chandra pulsar model; Table 1). The best-fit parameters for the PWN were inferred to be $N_{\text{H}} = (4.6 \pm 0.3) \times 10^{22} \text{ cm}^{-2}$, $\Gamma = 1.98 \pm 0.07$ and $F_{3-10 \text{ keV}} = (1.50 \pm 0.07) \times 10^{-13} \text{ erg cm}^{-2} \text{ s}^{-1}$. The cross-normalization factors for the NuSTAR FPMA and FPMB spectra with respect to the Chandra spectrum were slightly higher than, but consistent with 1 at the $\lesssim 2\sigma$ level. We also achieved an acceptable fit to the PWN spectra with a broken power law ($\chi^2/\text{dof}=324/315$). A comparison of the broken power-law and power-law fits found an f -test probability of 0.8, suggesting no significant evidence for spectral curvature or cut-off.

Note again that we used the `angr` abundances for the quoted N_{H} value, to compare to previously published studies and be consistent throughout. Using the newer `Wilms` abundances (Wilms et al. 2000) gives, as expected, a higher column density of $(6.94 \pm 0.55) \times 10^{22} \text{ cm}^{-2}$ but does not change the other spectral parameters.

Because the results may still be influenced by Chandra’s background, we checked them with the 10 Chandra background selections and found $1\text{-}\sigma$ variations of the parameters to be $\Delta N_{\text{H}} = \pm 0.4 \times 10^{22} \text{ cm}^{-2}$, $\Delta \Gamma = \pm 0.03$ and $\Delta F_{3-10 \text{ keV}} = \pm 2 \times 10^{-14} \text{ erg cm}^{-2} \text{ s}^{-1}$. The joint-fit results also vary depending on the NuSTAR background simulation and the pulsar model. Uncertainties due to the former and the latter were estimated to be $\Delta N_{\text{H}} = \pm 10^{21} \text{ cm}^{-2}$, $\Delta \Gamma = \pm 0.04$, and $\Delta F_{3-10 \text{ keV}} = \pm 10^{-14} \text{ erg cm}^{-2} \text{ s}^{-1}$ (1σ), and $\Delta N_{\text{H}} = \pm 10^{21} \text{ cm}^{-2}$, $\Delta \Gamma = {}_{-0.03}^{+0.06}$, and $\Delta F_{3-10 \text{ keV}} = \pm 10^{-14} \text{ erg cm}^{-2} \text{ s}^{-1}$ (min/max), respectively. These systematic uncertainties are combined in quadrature and reported in Table 1.

2.4.3. Chandra spectra of the sub-structures in the PWN

We measured the X-ray spectra of the sub-structures found in the Chandra image: the torus, jet, and northern tail (Fig. 2). The spectra of the other structures (e.g., knots) were difficult to measure due to the paucity of counts. To extract spectra, we used elliptical regions with sizes of $10'' \times 7''$ (excluding a $R = 2''$ region around the pulsar; Fig. 2a), $7'' \times 17''$ (Fig. 2b), and $2' \times 6'$ (Fig. 2c) for the torus, jet, and tail, respectively. Background spectra were extracted in the vicinity of the source regions. We then grouped the spectra to have at least 20 counts per bin and fit the spectra with absorbed power-law models holding N_{H} fixed at $4.6 \times 10^{22} \text{ cm}^{-2}$. The results are presented in Table 1.

2.4.4. Spatially resolved spectra of the PWN

The spectrum of the K3 PWN has been reported to soften with increasing distance from the pulsar from $\Gamma \approx 1.7\text{--}1.8$ to $2.1\text{--}2.3$ (Van Etten & Romani 2010;

Kishishita et al. 2012). Our image analysis result (Section 2.3.2) supported this softening. We further investigate the spectral softening with the Chandra and NuSTAR data by measuring spatially resolved spectra of the PWN. Because the source is not very bright, we use large extraction regions.

In the Chandra data, the source spectra were extracted from five annular regions: $R = 2\text{--}10''$, $10\text{--}50''$, $50\text{--}90''$, $90\text{--}130''$, and $130\text{--}180''$ centered on J1420. Background regions were chosen using the procedure described above (based on the blank-sky data and area fraction of the source region in the chips; Section 2.4.2). We grouped the spectra to have a minimum of 30 counts per bin and jointly fit them with an absorbed power-law model having an unlinked Γ for each spectrum and a common (and frozen) N_{H} of $4.6 \times 10^{22} \text{ cm}^{-2}$. We fit the data with 10 different background regions to estimate the systematic uncertainties (1σ variations of the best-fit parameters). The min-max variation of Γ was small in the innermost region ($\Delta \Gamma \leq 0.1$) but as large as $\Delta \Gamma \approx 0.6$ in outer regions. The flux variation was modest ($<10\%$). Because the Γ variations are substantial compared to the statistical uncertainties, we averaged the best-fit parameters and added their 1σ variations to the statistical uncertainties in quadrature; these are displayed in Figure 5 c and d. The Chandra constraint on the Γ profile is poor, and thus we rely on the Suzaku (Kishishita et al. 2012) and NuSTAR measurements (see below) of the Γ profile for our SED modeling (Section 3.2).

For the NuSTAR data, we used a $R = 1'$ circle and two annular regions with a width of $1'$ each, covering a $R = 3'$ circular region. Background spectra were generated with the `nuskybgd` simulations. As noted above, the off-pulse intervals are narrow, and thus we used all the phases and jointly modeled the pulsar emission. Its influence on the PWN spectrum decreases rapidly with distance from the pulsar due to the PSF effect, which was taken into account by reducing the normalization factor of the pulsar model according to the enclosed energy fraction of the PSF (e.g., An et al. 2014b) in each zone. We grouped the spectra to have at least 30 counts per spectral bin and jointly fit the spectra with power-law models having separate Γ s and a common N_{H} (frozen at $4.6 \times 10^{22} \text{ cm}^{-2}$). The fit was acceptable with $\chi^2/\text{dof}=385/371$, and the resulting best-fit parameters are presented in Figure 5 c and d. Note that systematic uncertainties (e.g., varying the pulsar model and `nuskybgd` simulations; Section 2.4.2) were added to the statistical uncertainties in quadrature. For the NuSTAR data, a model with a common Γ for the three spectra also yielded a good fit with $\chi^2/\text{dof}=391/373$. An f -test

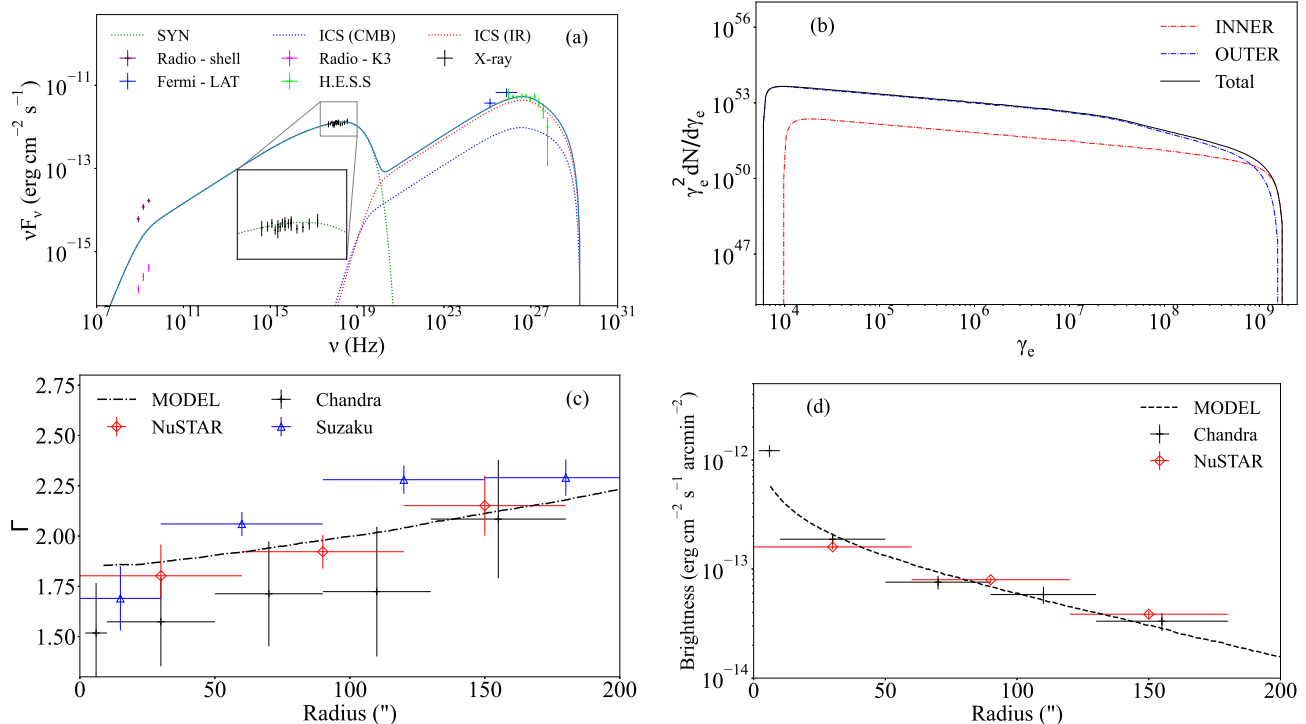


Figure 5. Broadband SED, radial profiles of X-ray photon index and brightness measured for the K3 PWN, and an optimized multi-zone emission model. (a) Spatially integrated broadband SED (Section 3.1) data and the optimized model. The radio points are the K3 excess (pink; Roberts et al. 1999) and the shell emission (purple; Van Etten & Romani 2010); we take these as the lower and upper limit, respectively, as was done by Van Etten & Romani (2010). The X-ray points are our measurements of the PWN emission within the $R = 2.5'$ region, and the blue and green points show >20 GeV Fermi-LAT data (Fermi-LAT collaboration et al. 2022) and the H.E.S.S. measurements taken from Aharonian et al. (2006), respectively. The curves are model-computed emission components: green for the synchrotron, red and blue for the ICS from IR and CMB seeds, and blue solid for the summed model. (b) Model-computed particle distributions in the inner ($r < 100''$; red) and the outer ($100'' < r < 150''$; blue) regions, and their sum (black), (c-d) radial profiles of X-ray photon index (c) and brightness (d). In panel (c), we also show Suzaku measurements (Kishishita et al. 2012) in blue for reference.

comparison of the common and separate Γ models found $p=0.07$, which is weakly suggestive of a spatial variation of Γ , possibly supporting the previous measurements of the spectral softening in K3 (Van Etten & Romani 2010; Kishishita et al. 2012). The NuSTAR-measured Γ values are slightly smaller than those measured by Suzaku, possibly because of the different PSF profiles and/or a cross-calibration issue (Madsen et al. 2015b).

3. MODELING OF THE PWN EMISSION

3.1. Broadband SED data

To investigate the properties of particle flow in the K3 PWN using a multi-zone emission model, we collected radio and TeV SED measurements from the literature (Roberts et al. 1999; Van Etten & Romani 2010; Aharonian et al. 2006) and took Fermi-LAT data from the 4FGL DR-3 catalog (Fermi-LAT collaboration et al. 2022). We then added them to our X-ray measurements to construct a broadband SED of the source (Fig. 5). Note that Van Etten & Romani (2010) regarded the radio measurements as upper limits for the radio emission of the PWN because an association between the X-ray

PWN and the apparent radio shell were not established. We also take the K3 excess and the shell emission as the lower and upper limits, respectively, for our SED analysis.

The K3 PWN was detected as an extended source (4FGL J1420.3–6046e) in the Fermi-LAT 4FGL DR-2 and DR-3 catalogs (e.g., `gll_psc.v28.fit`; Abdollahi et al. 2020; Fermi-LAT collaboration et al. 2022), and the bright gamma-ray pulsar J1420 is within the PWN. The nebular emission was modeled by a power law with photon index $\Gamma = 2.00 \pm 0.13$ and $\Gamma = 2.05 \pm 0.09$ (green in Fig. 6) in the DR-2 and DR-3 catalog, respectively. In our inspection of the LAT SEDs reported in the catalogs, we found that low-energy ($\lesssim 20$ GeV) flux points of the PWN exhibit a rapidly falling trend with increasing energy (two blue points at $\lesssim 20$ GeV in Fig. 6). This trend is reminiscent of the exponentially cut-off pulsar spectrum (red in Fig. 6). We suspect that some of the high-energy SED tail of the gamma-ray pulsar 4FGL J1420.0–6048 (LAT counterpart of J1420) was ascribed to the PWN model in the catalogs. This speculation is supported by the fact that the PWN is flagged

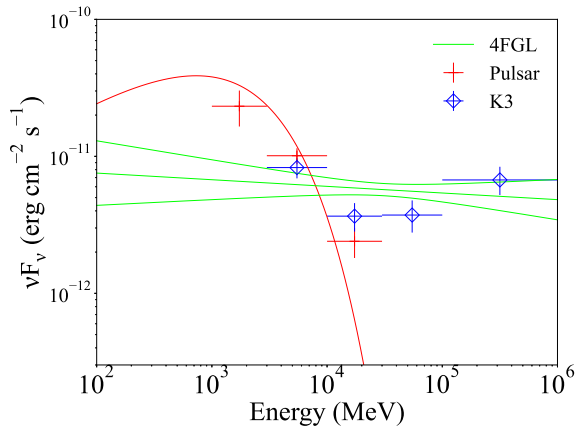


Figure 6. Fermi-LAT SEDs in the 100 MeV–1 TeV band (taken from the 4FGL DR-3 catalog). The pulsar’s SED points and the PLSuperExpCutoff4 (Fermi-LAT collaboration et al. 2022) model are shown in red, and the blue points are the measured SED of the PWN 4FGL J1420.3–6046e. The catalog model for the PWN is displayed in a green band.

as a ‘variable’ source probably because it was confused with J1420 as noted by Abdollahi et al. (2020). So we use only the >20 GeV SED points.

The broadband SED in the radio to VHE band is presented in Figure 5 a. Note that we adopted X-ray SED data from within $R = 2.5'$ (Section 2.4.2) and thus integrate our computed X-ray SEDs only out to that distance (see below).

3.2. Multi-zone PWN emission modeling

We applied our phenomenological multi-zone emission model (Kim & An 2020b) to the broadband SED and the measured X-ray profiles of photon index and brightness of K3. In the model, the pulsar supplies electrons and magnetic field B to the PWN. The spin-down power \dot{E}_{SD} of the pulsar goes into energies of the particles ($\dot{E}_e \equiv \eta_e \dot{E}_{\text{SD}}$) and B ($\dot{E}_B \equiv \eta_B \dot{E}_{\text{SD}}$) in the PWN, and the pulsar’s gamma-ray radiation ($L_\gamma \equiv \eta_\gamma \dot{E}_{\text{SD}}$). As was done in Gelfand et al. (2009), we assume \dot{E}_{SD} evolves over time following $\dot{E}_{\text{SD}}(t) = L_0 \left(1 + \frac{t}{\tau_0}\right)^{-\frac{n+1}{n-1}}$, where $\tau_0 = 2\tau_c/(n-1) - t_{\text{age}}$ and n is the braking index (assumed to be 3 in this work). We further assume a constant η_e , so \dot{E}_e also evolves with the same time dependence as \dot{E}_{SD} . Electrons with a power-law energy distribution, $dN_e/d\gamma_e dt = N_0 \gamma_e^{-p_1}$, are injected at the termination shock and flow in the PWN via advection and diffusion.

The emission model assumes a spherical flow whose properties, magnetic field strength B , flow speed V_{flow} , and diffusion coefficient D , are assumed to be power laws: $B(r) = B_0(r/R_{\text{TS}})^{\alpha_B}$, $V_{\text{flow}}(r) = V_0(r/R_{\text{TS}})^{\alpha_V}$, and $D = D_0(\gamma_e/10^9)(B/100\mu\text{G})^{-1}$, where R_{TS} is the

distance from the pulsar to the termination shock. These properties are time-independent in our model, but in reality are likely to change with time because of the time-dependent energy injection \dot{E}_{SD} (see Section 4.3). We estimate η_B by comparing the time-integrated \dot{E}_{SD} to the space-integrated magnetic energy density: $\eta_B \int_0^{t_{\text{age}}} \dot{E}_{\text{SD}} dt = 4\pi \int_{R_{\text{TS}}}^{R_{\text{PWN}}} (B^2/8\pi)r^2 dr$. η_γ is computed by comparing the measured L_γ to the present-day $\dot{E}_{\text{SD}}(t_{\text{age}})$. We then require $\eta_e + \eta_B + \eta_\gamma \lesssim 1$.

Particle evolution (in space and energy) is computed in 1000 spatial zones and $10^4 \gamma_e$ bins and for 10^5 time steps, considering radiative and adiabatic losses (e.g., Tang & Chevalier 2012). We compute the synchrotron and ICS spectra of the particles in each of the emission zones. For the ICS seed photons, we use the CMB ($T_{\text{CMB}} = 2.7\text{K}$ with energy density $u_{\text{CMB}} = 0.26 \text{ eV cm}^{-3}$) and IR (T_{IR} with energy density u_{IR}) radiation; the parameters for the latter are adjusted to match the VHE SED. We project the computed emission onto the tangent plane of the observer, construct spatially integrated and resolved SEDs, and compare them with measurements (e.g., Fig. 5). For the comparison, we integrate the model emission over the projected areas appropriate for the SED measurements (i.e., $2.5'$ for X-ray and 0.12° for VHE). Note that the Fermi LAT measured the size of the K3 PWN to be 0.123° using a disk model, whereas H.E.S.S. measured it to be 0.08° using a Gaussian model (1σ width). In this work, we adopt the LAT-measured size, but a different size could be accommodated by our model with a change of u_{IR} .

Since there are many covariant parameters, it is infeasible to determine all of them with the given measurements of the broadband SED and radial profiles. We, therefore, make some assumptions about the PWN flow. For B , we assume transverse configuration (e.g., Bucciantini et al. 2022) and magnetic flux conservation: i.e., $\alpha_V + \alpha_B = -1$ (Reynolds 2009). We further assume an age of $t_{\text{age}} = 9\text{kyr}$ based on the gamma-ray-to-X-ray flux ratio (see Kargaltsev et al. 2013), and $R_{\text{TS}} = 0.14\text{pc}$ and $R_{\text{PWN}} = 10.75\text{pc}$ according to the torus size ($\sim 5''$) and the VHE size of the PWN (0.12°), respectively, for an assumed distance of $d = 5.6\text{kpc}$. As the X-ray emission seems to be confined within a certain radius from the pulsar, the PWN properties (B and V_{flow}) may change abruptly at the boundary. We verified that the model-computed emissions did not alter much whether or not we used such abrupt changes in our modeling since the predicted brightness is very low in the outer regions (e.g., Fig. 5 d).

Some of the model parameters can be roughly estimated based on the observations. As Klein-Nishina suppression for electron scattering from IR and CMB seed

Table 2. Parameters for the multizone SED model

Parameter	Symbol	Value
Spin-down power	\dot{E}_{SD}	$10^{37} \text{ erg s}^{-1}$
Characteristic age of the pulsar	τ_c	13000 yr
Age of the PWN	t_{age}	9000 yr
Size of the PWN	R_{pwn}	10.75 pc
Radius of termination shock	R_{TS}	0.14 pc
Distance to the PWN	d	5.6 kpc
Index for the particle distribution	p_1	2.33
Minimum Lorentz factor	$\gamma_{e,\text{min}}$	$10^{4.45}$
Maximum Lorentz factor	$\gamma_{e,\text{max}}$	$10^{9.24}$
Magnetic field	B_0	$5.1 \mu\text{G}$
Magnetic index	α_B	-0.06
Flow speed	V_0	$0.14c$
Speed index	α_V	-0.94
Diffusion coefficient	D_0	$1.2 \times 10^{26} \text{ cm}^2 \text{ s}^{-1}$
Energy fraction injected into particles	η_e	0.9
Energy fraction injected into B field	η_B	0.007
Temperature of IR seeds	T_{IR}	10 K
Energy density of IR seeds	u_{IR}	1.7 eV cm^{-3}
CMB temperature	T_{CMB}	2.7 K
CMB energy density	u_{CMB}	0.26 eV cm^{-3}

photons is expected at $\gtrsim 100 \text{ TeV}$, the ICS emission of K3 occurs mostly in the Thomson regime. Then, for the observed ICS to synchrotron SED peak ratio of ~ 4 and an assumed u_{IR} in the Galaxy of $\approx 1 \text{ eV cm}^{-3}$, $\frac{B^2}{8\pi} \approx \frac{u_{\text{IR}} + u_{\text{CMB}}}{4}$ gives $B \approx 4 \mu\text{G}$. For this B , $\approx 20 \text{ keV}$ photons observed from K3 imply a maximum γ_e of $\approx 5 \times 10^8$. The uncooled spectrum of the electrons can be directly inferred from the IR-to-optical (synchrotron) and the LAT (ICS) SEDs. With the lack of IR/optical measurements, a LAT photon index of ≈ 1.7 measured by differencing the two $>20 \text{ GeV}$ LAT points (Fig. 6) implies a $p_1 = 2\Gamma - 1$ of ≈ 2.4 .

Using the aforementioned estimates as a guide, we optimized the model to match the broadband SED and radial profiles of the X-ray brightness and photon index. An optimized model is displayed in Figure 5 with parameters given in Table 2. We found that particle transport is dominated by advection which carries the particles to $\sim 12 \text{ pc}$ over the age of 9 kyr as compared to the diffusion length $2\sqrt{Dt_{\text{age}}}$ of $\approx 2 \text{ pc}$ and $\approx 5 \text{ pc}$ for VHE (e.g., $\gamma_e \approx 10^7$) and X-ray emitting (e.g., $\gamma_e \approx 10^8$) electrons, respectively. The diffusion length scale for the highest-energy electrons ($\gamma_e \approx 10^9$) is comparable to the advection length scale.

In our model, the most energetic particles in K3 have energies of $\approx 10^{15} \text{ eV}$ and cool substantially via synchrotron emission over the pulsar's age (Fig. 5 b). Therefore, the synchrotron spectra in outer regions are softer than those in inner regions (i.e., spectral softening by synchrotron burn-off effects). The computed radial profiles of Γ and brightness depend sensitively on the

flow properties (e.g., B , α_B , D_0 , etc.) and thus provide crucial information on the model parameters. For example, a model with a large B or α_B has difficulty accommodating the large X-ray/VHE extension of the source ($\approx 10 \text{ pc}$) because particles would have cooled efficiently via synchrotron radiation in the inner zones, giving fainter emission at large distances. In contrast, a model with a smaller B would make the Γ and brightness profiles flatter. Moreover, such a low- B model requires more particles (i.e., larger η_e) to match the observed SED. Then the observed $\dot{E}_{\text{SD}} = 10^{37} \text{ erg s}^{-1}$ of J1420 may be insufficient to provide the required amount of particles; i.e., $\eta_e + \eta_B + \eta_\gamma > 1$ for a measured η_γ of $\approx 7\%$ for J1420.

The VHE emission primarily arises from the ICS from the IR seeds (Fig. 5 a) by electrons with energies of $\approx 10 \text{ TeV}$. The H.E.S.S. flux ($> \text{TeV}$) is lower than (but within uncertainties of) the LAT flux ($< 1 \text{ TeV}$), possibly indicating a cross-calibration issue. We adjusted our model to match the H.E.S.S. measurements because they have smaller uncertainties. Our model slightly overpredicts the $>10 \text{ TeV}$ SED points, especially the highest-energy one. It may be due to statistical fluctuations, but if real, the highest-energy measurement is hard to explain with our simple model. As the ICS emission at the highest energies is mainly produced in inner regions (see Section 4.3), reducing the IR seeds in those regions may help to reconcile the small discrepancy. Note that the u_{IR} value we used is higher than the Galactic average dust emission (e.g., Vernetto & Lipari 2016) but is similar to values inferred for other PWNe (e.g., Torres et al. 2014) as PWNe are in crowded regions.

4. DISCUSSION

4.1. The pulsar J1420 and the K3 PWN

It was firmly established by a Chandra image (Ng et al. 2005) and detection of radio and gamma-ray pulsations (D'Amico et al. 2001; Weltevrede et al. 2010) that J1420 is associated with the K3 PWN. The energetic pulsar ($\dot{E}_{\text{SD}} = 10^{37} \text{ erg s}^{-1}$) has a power-law spectrum with a photon index $\Gamma = 0.7$ and a flux $F_{3-10\text{keV}} = 1.3 \times 10^{-13} \text{ erg cm}^{-2} \text{ s}^{-1}$ which corresponds to a 3–10 keV X-ray luminosity of $\approx 5 \times 10^{32} \text{ erg s}^{-1}$ for the assumed distance of 5.6 kpc. For its $f = 14.66 \text{ Hz}$ and $\dot{f} = -1.77 \times 10^{-11} \text{ Hz s}^{-2}$, the measured emission properties of J1420 appear to accord with correlations seen in rotation-powered pulsars (RPPs) between temporal and emission properties: e.g., correlations of Γ and X-ray luminosity $L_{\text{X,PSR}}$ with \dot{E}_{SD} , τ_c , $P = 1/f$, and $\dot{P} = -\dot{f}/f^2$ (e.g., Li et al. 2008). The measured properties of J1420 and K3 are also in accordance with cor-

relations found between properties of other RPP/PWN systems; e.g., Γ and X-ray luminosity $L_{X,pwn}$ of PWNe are correlated with P , \dot{P} , τ_c , \dot{E}_{SD} , Γ and $L_{X,PSR}$ of the pulsars (Gotthelf 2003; Li et al. 2008). So we conclude that J1420/K3 is not significantly different from other RPP/PWN systems.

Using the XMM-Newton and NuSTAR data, we unambiguously detected the X-ray pulsations of J1420 up to 30 keV (Section 2.2), which supports the idea that J1420 is a soft γ -ray pulsar as suggested by Kuiper & Hermsen (2015). The X-ray pulse profile of J1420, with a sharp peak and a broad bump, is similar to that of another soft γ -ray pulsar PSR J1418–6058. Intriguingly, these two pulsars seem to exhibit similar gamma-ray pulse profiles having a smaller peak followed by a bridge and a brighter peak.⁹ In the case of PSR J1418–6058, the sharp X-ray peak phase-aligns with the smaller gamma-ray peak (Kim & An 2020a), but the X-ray and gamma-ray phase alignment is unclear in the case of J1420 because the existing LAT timing solution does not cover the X-ray epochs. As the relative phasing can provide clues to the spin orientation of the pulsar, further LAT timing studies are warranted.

4.2. The PWN morphology

In the Chandra data, we identified several small-scale X-ray features: knots and a torus-jet structure. Although ‘Knot 1’ may be a point source overlapping with the torus by chance, no detection of an IR or optical counterpart in the 2MASS and USNO catalogs within $< 5''$ and a rather broad spatial distribution observed for Knot1 (compared to other point sources with similar counts) suggest that it may be a diffuse PWN. If so, we may speculate based on its location (near the jet base) that Knot 1 may correspond to a dynamical feature near the jet base similar to those seen in the Crab nebula (e.g., Hester et al. 2002). Knot 2 is also close to the jet but not well aligned with it. Hence, the nature of Knot 2 remains uncertain.

The torus-jet structure we found (Fig. 2 a) can be interpreted as the termination shock (e.g., Ng et al. 2005) and a collimated jet. The torus radius of $\sim 5''$ corresponds to 0.14 pc for the assumed distance of 5.6 kpc and is consistent with the size of a termination shock formed by pressure balance (e.g., Kargaltsev & Pavlov 2008). So the termination shock interpretation of the torus is plausible. Then the spin orientation of J1420 may be inferred by a torus model (Ng & Romani 2004); the directions of the torus and the jet suggest that the position angle of the spin axis is $\approx 40^\circ$ east from the

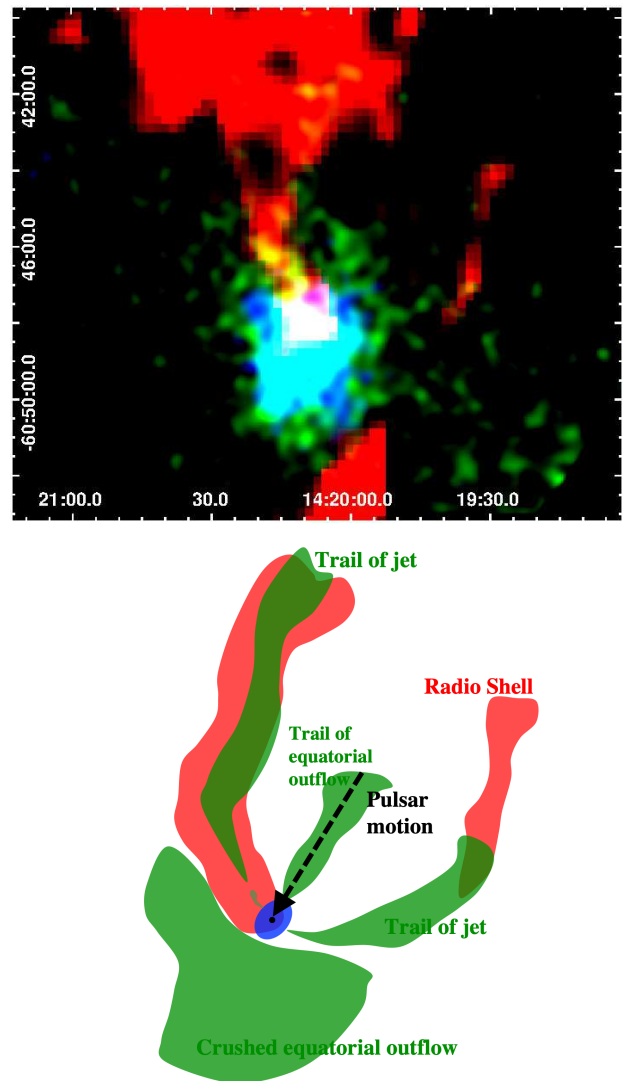


Figure 7. A false-color image of the source (top) and a schematic (bottom) that shows our speculation on the emission components. (Top) A radio and X-ray image of the PWN: red for the SUMSS 843 GHz, green for the Chandra 1–7 keV, and blue for the NuSTAR 3–20 keV image (see Figs. 2 and 3). (Bottom) Structures (tails and southern bright region) seen in the Chandra image are presented in green, and the apparent radio shell structure seen in the SUMSS image is depicted in red. The black dotted arrow shows a suggested pulsar’s trajectory (e.g., Van Etten & Romani 2010).

north (i.e., along the jet), and an aspect ratio of ~ 0.6 – 0.7 of the torus morphology may suggest that the spin-axis is ~ 35 – 45° into or out of the tangent plane if the torus is a ring as is observed in the Crab Nebula. Further, the fact that a southern jet is not detected may imply that the northern jet is pointing out of the plane. These crude estimates need to be updated by more precise torus modeling (e.g., Ng & Romani 2004), which

⁹ https://www.slac.stanford.edu/~kerrm/fermi_pulsar_timing/

can be further checked with pulse profile modeling (e.g., Harding & Muslimov 1998; Romani & Watters 2010).

The long northern tail detected by Suzaku was interpreted as a trail of the pulsar which had been born 3' northwest at the center of an apparent radio shell (Van Etten & Romani 2010, see also Fig. 7). In this scenario, the three tails in the Chandra image (Fig. 2 c) may be related to the pulsar's polar and equatorial outflows (Fig. 7 bottom) analogous to those observed in Geminga (Posselt et al. 2017). In this picture, the much more prominent (top) tail ('Tail' in Fig. 2 c) is the bent, originally approaching polar jet, the middle tail is the equatorial outflow, and the bottom tail is the bent counter jet (Fig. 7 bottom). The putative radio shell discovered by Van Etten & Romani (2010) might be compressing the PWN in the south-east, and the narrow inner jets (Fig. 2 middle) might have been blocked by the shell, turning into the broad tails over the course of the pulsar's motion (e.g., Fig. 7 bottom). The compressed southern region would have stronger magnetic field and hence brighter synchrotron emission. Then particles in the south would cool rapidly via the synchrotron process, and their VHE emission would be extended in the other direction, perhaps accounting for the offset VHE emission. Alternatively, if the pulsar's motion is very small, one can speculate that the irregular morphology might be caused by inhomogeneities in the ambient medium (e.g., asymmetric reverse shock interaction; Van Etten & Romani 2010). These scenarios can be distinguished by a measurement of the pulsar's proper motion. In the bent outflow scenario, the pulsar is expected to move $0.014''(13\text{kyr}/t_{\text{age}})\text{ yr}^{-1}$ in the south-east direction; a future high-resolution observatory (e.g., Lynx or AXIS; Gaskin et al. 2019; Mushotzky et al. 2019) might be able to detect this proper motion with a $\gtrsim 20$ -yr baseline (e.g., in 2030s).

It is intriguing to note that no significant radio emission coinciding with the bright X-ray emission is seen in the southern region. In contrast to K3, other young or middle-aged PWNe exhibit morphological similarity in the radio and X-ray bands (Ng et al. 2005; Matheson & Safi-Harb 2010). It is unclear what causes the lack of radio emission in K3, but it implies that both B and particle energies are high in the south of K3 so that the electrons emit synchrotron radiation above the radio band. These may be related to a reverse shock interaction. If so, we may speculate that the reverse shock interaction started rather recently, and thus the electrons have not cooled sufficiently to produce significant radio emission; i.e., the synchrotron peak frequency $\nu_{\text{SY}} \propto B\gamma_{e,\text{min}}^2$ lies above the $\sim\text{GHz}$ radio band.

4.3. SED modeling

Although the multi-zone model reproduced the observed data broadly, the parameter values are not well constrained due to model assumptions and parameter covariance. In particular, it is clear that the K3 PWN has some sub-structures (Fig. 2) and is not spherically symmetric (Fig. 7). Moreover, the particle flow in the PWN may be very complex due to pulsar motion and reverse shock compression (e.g., Van Etten & Romani 2010, Section 4.2). Our model, with the assumptions of spherical flow, homogeneous IR seed photons and smooth particle distribution, does not take into account the complex morphology and flows in the bent outflow and/or compressed regions, which may introduce some inaccuracy to the parameter estimations; e.g., the $\alpha_B + \alpha_V = -1$ relation may not be valid. In addition, the PWN properties B and V_{flow} were assumed to be constant in time; these might be higher at early times as \dot{E}_{SD} was larger. This effect has some influence on the old particles in outer regions and would make their spectra softer than was predicted by our model. However, the broadband SED might be little affected since the X-ray emission from the outer zones is weak (e.g., Fig. 5). Note also that the complex parameter covariance of the SED model was not thoroughly investigated, and there are likely other sets of parameters that may explain the data equally well. Hence, the parameters reported in Table 2 may represent only the average properties and need to be taken with caution. Nonetheless, we discuss below a few intriguing parameters inferred from the modeling.

The spectral softening demands a reasonably strong B , but if it is too strong the model-predicted brightness profile drops too rapidly with increasing distance to match the measured X-ray profiles. Our model-inferred $B_0 \approx 5\mu\text{G}$ is comparable to those inferred from a one-zone ($3\text{--}4\mu\text{G}$; Kishishita et al. 2012; Zhu et al. 2018) or a two-zone model ($8\mu\text{G}$; Van Etten & Romani 2010). We further found that the magnetic index α_B is also small (-0.06), meaning that B in the PWN does not vary much spatially. The particle motion is mainly driven by the bulk motion V_{flow} and for the assumed age of 9 kyr, $V_0 = 0.14c$ and $\alpha_V = -0.94$ ($V \sim 1/r$) are sufficient to carry the particles to the outer boundary of the PWN. These model parameters as well as the hard X-ray emission of K3 suggest that electrons are accelerated to very high energies ($\approx 1\text{ PeV}$) in the system.

The inferred parameters for the K3 PWN are generally similar to those for the middle-aged Rabbit PWN associated with PSR J1418–6058, which has a similar τ_c (10 kyr) to J1420's, but the diffusion coefficients D_0 differ by an order of magnitude because their observed radial profiles of Γ are very different (Park et al. sub-

mitted). X-ray spectral softening was insignificant in the Rabbit PWN and thus a large value of D_0 was required by the model to homogenize the effects of synchrotron cooling. An alternative explanation for the lack of softening, negligible diffusion, required an unreasonably low value of B to avoid a sharp spectral cutoff before the edge of the nebula (see below). For the D_0 values inferred for the two PWNe, the primary particle transport mechanisms were also inferred to differ: advection-dominant for K3 and diffusion-dominant for Rabbit. Note, however, that for the highest-energy particles ($\gamma_e \approx 10^9$) the effect of diffusion is comparable to that of advection even in K3. While the parameters inferred by our phenomenological model may not be accurate, the distinctions (i.e., Γ profiles) observed between the two PWNe convincingly suggest that their diffusion properties differ. This may be related to the evolution of the PWNe, and their interaction with the putative supernova remnants and/or the ambient medium. These need to be investigated with more physically-motivated evolution models.

Although the particle transport in K3 is dominated by advection, the mild and steady increase of Γ with distance is different from those expected in purely advective flows. In these cases, all the particles at a certain radius have the same age (cooling time). So in inner regions, where the cooling break is above X-ray energies, the synchrotron spectral index in the X-ray band does not change radially. As the particles propagate outward in the later evolutionary stage, the cooling break moves to lower energies, eventually to X-rays. From that radius the X-ray spectrum softens rapidly with increasing radius (age). This trend is almost universally observed in 1D pure-advection models (e.g., Reynolds 2003). Such a trend can turn into a steadily increasing one (observed in K3) if particles of different ages can mix. This can be achieved by non-radial backflows that bring older (outer) particles back into the inner regions and/or by diffusion. Although the former may play a role in K3 (e.g., in the southern region), the details of the backflows are not well known and thus difficult to incorporate into our spherically symmetric model. Hence, we relied on particle diffusion in this work. For the X-ray emitting electrons, the diffusion length scale in K3 was estimated to be ~ 5 pc (or longer for the highest-energy electrons) which is sufficient to mix particles of various ages (c.f., 12 pc for advection). Note that Tang & Chevalier (2012) demonstrated that Γ profiles flatten at large distances in models with reflecting outer boundary conditions probably by producing backflows, whereas Γ steadily increases with distance in the absence of the backflow (i.e., transmitting outer

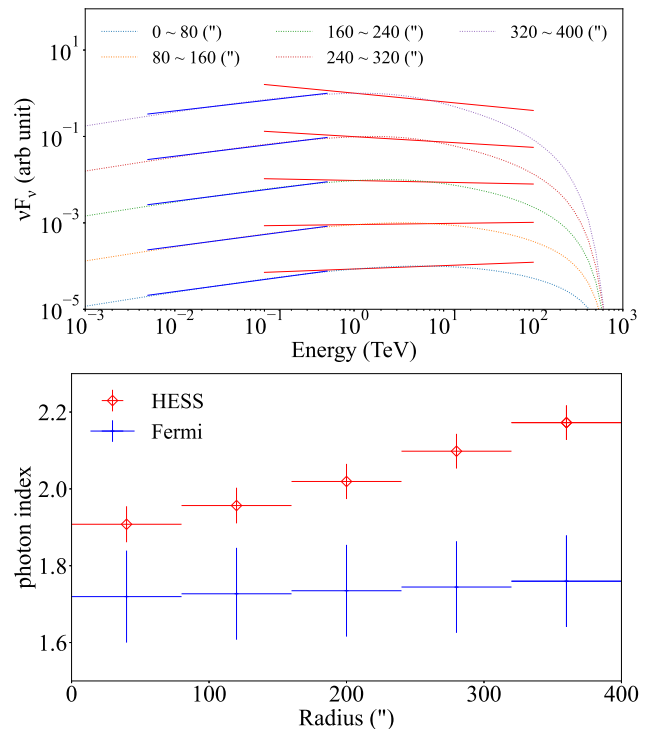


Figure 8. Spatially resolved VHE SED models and effective photon indices computed with the model fluxes. (*Top*) VHE SEDs from an inner (bottom) to an outer (top) region. The SEDs are displaced in the y-axis for legibility. The straight lines drawn on the SEDs are effective power-law fits to simulated SED data that are constructed using the model-computed fluxes and relative uncertainties on the spatially integrated LAT and H.E.S.S. SED measurements. (*Bottom*) Photon indices of the effective power-law models in the LAT (blue) and the H.E.S.S. (red) bands. See text for more detail.

boundary). The Suzaku measurement of the Γ profile of K3 seems to exhibit a flattening (Fig. 5), but a better measurement with finer radial bins is needed to confirm it.

Our model predicts a cooling break at $\gamma_e \approx 10^7$. Because particles with that Lorentz factor emit ICS radiation at ≈ 1 TeV, spatial variation of emission below (i.e., LAT band) and above it (i.e., H.E.S.S. band) are expected to be substantially different as is demonstrated in Figure 8 which displays model-predicted VHE SEDs and effective photon indices in the LAT and H.E.S.S. bands. Note that this is only for demonstration, and the actual uncertainties on the spatially resolved SED points would vary depending on the instrument and exposure. The slope of the LAT SED does not vary spatially because the < 1 TeV emission is produced by uncooled electrons, whereas the cooling effect is clearly visible in the TeV band. Our model predicts a significant spectral softening in the H.E.S.S. band at a similar level to that seen in the X-ray band (Fig. 5 c). This can be tested with

deeper VHE observations of the source (e.g., by CTA; Actis et al. 2011).

5. SUMMARY

We analyzed broadband X-ray data to characterize the emission properties of J1420 and K3. Below we summarized our findings.

- We confidently detected the X-ray pulsations of J1420, using NuSTAR and XMM-Newton, and measured its pulse profile accurately.
- We identified sub-structures of the K3 PWN in the Chandra image: two knots, a torus-jet structure, and large-scale tails.
- Using NuSTAR images, we found a hint of a spectral softening with increasing distance from J1420. This is in accord with the previous measurements of the spectral softening in K3 (Van Etten & Romani 2010; Kishishita et al. 2012).
- Our multi-zone emission modeling suggested that particles are accelerated to very high energy (≈ 1 PeV), the nebular magnetic field is low ($B \sim 5\mu\text{G}$), and the particles are transported primarily by advection in the K3 PWN.

The high-quality X-ray data, especially those taken with NuSTAR thanks to its hard X-ray coverage, were useful for our study of the particle properties in the K3 PWN at the highest energies. A spectral cut-off was not detected to ~ 20 keV, implying that there may exist even higher-energy particles in the PWN; these can be probed by future observatories operating above the NuSTAR band (e.g., FORCE, HEX-P and COSI; Nakazawa et al. 2018; Madsen et al. 2019; Tomsick et al. 2019). Comparisons with other middle-aged PWNe can help to further our understanding of

PWN physics (e.g., Kargaltsev et al. 2013; Mori et al. 2021). For example, X-ray spectral softening has been observed in K3, but not in the Rabbit PWN; this was attributed to different levels of diffusion in our model. However, there may be other reasons (different evolution or environments) that the current data and models do not capture. Further observational and theoretical efforts are needed. Importantly, a measurement of the pulsar proper motion is needed to confirm the evolutionary scenario of this complex system.

This work used data from the NuSTAR mission, a project led by the California Institute of Technology, managed by the Jet Propulsion Laboratory, and funded by NASA. We made use of the NuSTAR Data Analysis Software (NuSTARDAS) jointly developed by the ASI Science Data Center (ASDC, Italy) and the California Institute of Technology (USA). This research was supported by Basic Science Research Program through the National Research Foundation of Korea (NRF) funded by the Ministry of Science, ICT & Future Planning (NRF-2022R1F1A1063468). Support for this work was partially provided by NASA through NuSTAR Cycle 6 Guest Observer Program grant NNH19ZDA001N. SSH acknowledges support from the Natural Sciences and Engineering Research Council of Canada (NSERC) through the Discovery Grants and Canada Research Chairs programs and from the Canadian Space Agency (CSA). We thank the referee for detailed comments that helped improve the clarity of the paper.

Facilities: CXO, XMM-Newton, NuSTAR

Software: HEASoft (v6.29; NASA High Energy Astrophysics Science Archive Research Center 2014), CIAO (v4.14; Fruscione et al. 2006), XMM-SAS (20211130.0941; Gabriel 2017), XSPEC (v12.12; Arnaud 1996)

REFERENCES

- Abdollahi, S., Acero, F., Ackermann, M., et al. 2020, ApJS, 247, 33
- Actis, M., Agnetta, G., Aharonian, F., et al. 2011, Experimental Astronomy, 32, 193
- Aharonian, F., Akhperjanian, A. G., Bazer-Bachi, A. R., et al. 2006, A&A, 456, 245
- An, H. 2019, ApJ, 876, 150
- An, H., Madsen, K. K., Reynolds, S. P., et al. 2014a, ApJ, 793, 90
- An, H., Madsen, K. K., Westergaard, N. J., et al. 2014b, in Proc. SPIE, Vol. 9144, Space Telescopes and Instrumentation 2014: Ultraviolet to Gamma Ray, 91441Q
- Anders, E., & Grevesse, N. 1989, GeoCoA, 53, 197
- Arnaud, K. A. 1996, in Astronomical Society of the Pacific Conference Series, Vol. 101, Astronomical Data Analysis Software and Systems V, ed. G. H. Jacoby & J. Barnes, 17

- Atwood, W. B., Abdo, A. A., Ackermann, M., et al. 2009, *ApJ*, 697, 1071
- Bartalucci, I., Mazzotta, P., Bourdin, H., & Vikhlinin, A. 2014, *A&A*, 566, A25
- Bucciantini, N., Arons, J., & Amato, E. 2011, *MNRAS*, 410, 381
- Bucciantini, N., Ferrazzoli, R., Bachetti, M., et al. 2022, arXiv e-prints, arXiv:2207.05573
- Burgess, D. A., Mori, K., Gelfand, J. D., et al. 2022, *ApJ*, 930, 148
- D’Amico, N., Kaspi, V. M., Manchester, R. N., et al. 2001, *ApJL*, 552, L45
- de Jager, O. C., Raubenheimer, B. C., & Swanepoel, J. W. H. 1989, *A&A*, 221, 180
- Fermi-LAT collaboration, Abdollahi, S., Acero, F., et al. 2022, arXiv e-prints, arXiv:2201.11184
- Fruscione, A., McDowell, J. C., Allen, G. E., et al. 2006, in *Proc. SPIE*, Vol. 6270, Society of Photo-Optical Instrumentation Engineers (SPIE) Conference Series, 62701V
- Gabriel, C. 2017, in *The X-ray Universe 2017*, 84
- Gaskin, J. A., Swartz, D. A., Vikhlinin, A., et al. 2019, *Journal of Astronomical Telescopes, Instruments, and Systems*, 5, 021001
- Gelfand, J. D., Slane, P. O., & Zhang, W. 2009, *ApJ*, 703, 2051
- Giacinti, G., Mitchell, A. M. W., López-Coto, R., et al. 2020, *A&A*, 636, A113
- Gotthelf, E. V. 2003, *ApJ*, 591, 361
- H. E. S. S. Collaboration, Abdalla, H., Abramowski, A., et al. 2018, *A&A*, 612, A2
- Harding, A. K. 1996, *SSRv*, 75, 257
- Harding, A. K., & Muslimov, A. G. 1998, *ApJ*, 500, 862
- Hester, J. J., Mori, K., Burrows, D., et al. 2002, *ApJL*, 577, L49
- Kargaltsev, O., & Pavlov, G. G. 2008, in *American Institute of Physics Conference Series*, Vol. 983, 40 Years of Pulsars: Millisecond Pulsars, Magnetars and More, ed. C. Bassa, Z. Wang, A. Cumming, & V. M. Kaspi, 171–185
- Kargaltsev, O., Rangelov, B., & Pavlov, G. 2013, in *The Universe Evolution: Astrophysical and Nuclear Aspects*. Edited by I. Strakovsky and L. Blokhintsev. Nova Science Publishers, 359–406
- Kennel, C. F., & Coroniti, F. V. 1984, *ApJ*, 283, 694
- Kerr, M. 2011, *ApJ*, 732, 38
- Kerr, M., Ray, P. S., Johnston, S., Shannon, R. M., & Camilo, F. 2015, *ApJ*, 814, 128
- Kim, M., & An, H. 2020a, *ApJ*, 892, 5
- Kim, S., & An, H. 2020b, *Astronomische Nachrichten*, 341, 170
- Kishishita, T., Bamba, A., Uchiyama, Y., Tanaka, Y., & Takahashi, T. 2012, *ApJ*, 750, 162
- Klein, O., & Nishina, T. 1929, *Zeitschrift fur Physik*, 52, 853
- Kuiper, L., & Hermsen, W. 2015, *MNRAS*, 449, 3827
- Lhaaso Collaboration, Cao, Z., Aharonian, F., et al. 2021, *Science*, 373, 425
- Li, X.-H., Lu, F.-J., & Li, Z. 2008, *ApJ*, 682, 1166
- Loredo, T. J. 1992, in *Statistical Challenges in Modern Astronomy*, ed. E. D. Feigelson & G. J. Babu, 275–297
- Madsen, K., Hickox, R., Bachetti, M., et al. 2019, in *Bulletin of the American Astronomical Society*, Vol. 51, 166
- Madsen, K. K., Reynolds, S., Harrison, F., et al. 2015a, *ApJ*, 801, 66
- Madsen, K. K., Harrison, F. A., Markwardt, C. B., et al. 2015b, *ApJS*, 220, 8
- Matheson, H., & Safi-Harb, S. 2010, *ApJ*, 724, 572
- Mauch, T., Murphy, T., Buttery, H. J., et al. 2003, *MNRAS*, 342, 1117
- Mori, K., An, H., Burgess, D., et al. 2021, arXiv e-prints, arXiv:2108.00557
- Mushotzky, R., Aird, J., Barger, A. J., et al. 2019, in *Bulletin of the American Astronomical Society*, Vol. 51, 107
- Nakazawa, K., Mori, K., Tsuru, T. G., et al. 2018, in *Society of Photo-Optical Instrumentation Engineers (SPIE) Conference Series*, Vol. 10699, Space Telescopes and Instrumentation 2018: Ultraviolet to Gamma Ray, ed. J.-W. A. den Herder, S. Nikzad, & K. Nakazawa, 106992D
- NASA High Energy Astrophysics Science Archive Research Center (Heasarc). 2014, HEASoft: Unified Release of FTOOLS and XANADU, ascl:1408.004
- Ng, C. Y., Roberts, M. S. E., & Romani, R. W. 2005, *ApJ*, 627, 904
- Ng, C. Y., & Romani, R. W. 2004, *ApJ*, 601, 479
- Nynka, M., Hailey, C. J., Reynolds, S. P., et al. 2014, *ApJ*, 789, 72
- Posselt, B., Pavlov, G. G., Slane, P. O., et al. 2017, *ApJ*, 835, 66
- Reynolds, S. P. 2003, arXiv e-prints, arXiv:0308483
- . 2009, *ApJ*, 703, 662
- . 2016, *Journal of Plasma Physics*, 82, 635820501
- Roberts, M. S. E., & Romani, R. W. 1998, *ApJ*, 496, 827
- Roberts, M. S. E., Romani, R. W., & Johnston, S. 2001a, *ApJL*, 561, L187

- Roberts, M. S. E., Romani, R. W., Johnston, S., & Green, A. J. 1999, *ApJ*, 515, 712
- Roberts, M. S. E., Romani, R. W., & Kawai, N. 2001b, *ApJS*, 133, 451
- Romani, R. W., & Watters, K. P. 2010, *ApJ*, 714, 810
- Tang, X., & Chevalier, R. A. 2012, *ApJ*, 752, 83
- Tomsick, J., Zoglauer, A., Sleator, C., et al. 2019, in *Bulletin of the American Astronomical Society*, Vol. 51, 98
- Torres, D. F., Cillis, A., Martín, J., & de Oña Wilhelmi, E. 2014, *Journal of High Energy Astrophysics*, 1, 31
- Van Etten, A., & Romani, R. W. 2010, *ApJ*, 711, 1168
- Verner, D. A., Ferland, G. J., Korista, K. T., & Yakovlev, D. G. 1996, *ApJ*, 465, 487
- Vernetto, S., & Lipari, P. 2016, *PhRvD*, 94, 063009
- Weltevrede, P., Abdo, A. A., Ackermann, M., et al. 2010, *ApJ*, 708, 1426
- Wik, D. R., Hornstrup, A., Molendi, S., et al. 2014, *ApJ*, 792, 48
- Wilms, J., Allen, A., & McCray, R. 2000, *ApJ*, 542, 914
- Zhu, B.-T., Zhang, L., & Fang, J. 2018, *A&A*, 609, A110